ResearchGate

See discussions, stats, and author profiles for this publication at: https://www.researchgate.net/publication/331034186

Salt Polygons are Caused by Convection

Preprint · February 2019

CITATIONS
0

READS
349

5 authors, including:

Jana Lasser
Complexity Science Hub Vienna
18 PUBLICATIONS **43** CITATIONS

SEE PROFILE

Joanna Nield
University of Southampton
35 PUBLICATIONS **751** CITATIONS

SEE PROFILE

Marcel Ernst
Universität Kassel
6 PUBLICATIONS **3** CITATIONS

SEE PROFILE

Some of the authors of this publication are also working on these related projects:

Project Emotion dynamics and depression View project

Project Trace element determination via high sensitivity Laser Ablation Sector Field ICP-MS View project

All content following this page was uploaded by Jana Lasser on 24 April 2019.

The user has requested enhancement of the downloaded file.

Salt Polygons are Caused by Convection

Jana Lasser,[1,2,*] Joanna M. Nield,[3] Marcel Ernst,[1,2] Volker Karius,[4] and Lucas Goehring[5,†]

[1] *Max Planck Institute for Dynamics and Self-Organization, Am Fassberg 17, 37077 Göttingen, Germany*
[2] *Institute for Nonlinear Dynamics, Georg-August-University Göttingen, Friedrich-Hund-Platz 1, 37077 Göttingen, Germany*
[3] *Geography and Environment, University of Southampton, Highfield, Southampton SO17 1BJ, UK*
[4] *Geowissenschaftliches Zentrum, Georg-August-University, Goldschmidtstrasse 3, 37077 Göttingen, Germany*
[5] *School of Science and Technology, Nottingham Trent University, Nottingham NG11 8NS, UK*

(Dated: February 12, 2019)

From fairy circles to patterned ground and columnar joints, natural patterns spontaneously appear in many complex geophysical settings. Here, we consider the origins of polygons in the crusts of salt playa and salt pans. These beautifully regular features, a meter or so in diameter, have a worldwide distribution and are important to the transport of salt and dust in arid regions, yet there has been no convincing mechanism known for their formation. We present the first evidence that they are the surface expression of buoyancy-driven convection in the porous soil beneath a salt crust. By combining consistent results from direct field observations, analogue experiments, linear stability theory, and numerical simulations, we further explain the conditions under which salt polygons will form, as well as how their characteristic size emerges.

arXiv:1902.03600v1 [nlin.PS] 10 Feb 2019

I. INTRODUCTION

Salt deserts are among the most inhospitable places of our planet, yet their otherworldly shapes and features inspire the imagination [1], and are an important drive of many climate processes. Among their most prominent features are characteristic hexagonal polygons, formed by ridges in the salt encrusted surface. These polygons can be found in salt pans around the world, from the Salar de Uyuni in Chile or the Chott el Djerid in Tunisia [2] to Badwater Basin and Owens Lake in California (Fig. 1) - always expressing the same size of about one meter.

Salt crusts are dynamic on the timescale of months to years [3, 4] and their driving mechanism is still unknown. Wind over these crusts creates dust, the emission of which forms a significant proportion of our global atmospheric dust production [5, 6] as well as a source of mineral transport to the oceans [7]. Dust from the surface of the dry Owens Lake has posed a major health problem for people living downwind of the lake [8–11], and is now the site of an intense remediation effort. Salt crusts also modify evaporation and heat flux from the playa surface [12]. It is important to understand the contribution of salt deserts to model the earth's water and energy balance.

Previous studies of salt playa have either focused solely on the crusts, patterns in which have been interpreted as wrinkles [13, 14] or cracks [15, 16], or on the dynamics of subsurface flows [17–20]. Here, we propose a new way of modeling the dynamics of salt playa, which couples the crust to the ground beneath it, and encompasses the system as a whole. We combine data from numerical simulations, experiments and the field to unequivocally prove that the polygonal salt patterns are caused by convection in the soil below. This three-dimensional, dynamical process in the subsurface is driven by the evaporation of water through the surface which in turn causes a stratified salt concentration distribution which is prone to a convective instability.

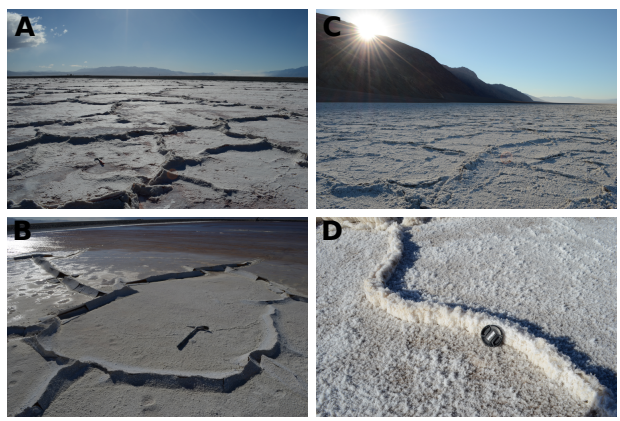

FIG. 1. Polygons formed by salt ridges at **A**, **B** Owens Lake and **C**, **D** Badwater Basin in Death Valley, both California.

To this end, we investigated salt polygons at Owens Lake (Fig. 1 **A** and **B**), a terminal saline lake covering about 25×15 kilometers, and Badwater Basin (Fig. 1 **C** and **D**). Most observations were made at Owens Lake, where the aquifer extends from the near-surface to at least 150 m depth [21]. It is subject to periodic flooding due to meltwater from the surrounding mountains, precipitation events and human controls of the water table. The groundwater carries dissolved salts [11, 22], which have collected in the evaporite pan [21]. Since 2000, the Los Angeles Department for Land and Water has undertaken major efforts to control dust emission from the lake-bed via shallow flooding [23], vegetation controls

* jana.lasser@ds.mpg.de
† lucas.goehring@ntu.ac.uk

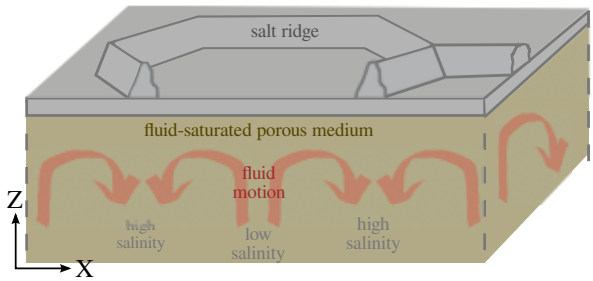

FIG. 2. Illustration of the proposed fluid dynamics in saturated porous soil beneath a patterned salt crust. Evaporation leaves the near-surface fluid enriched in salt, and heavier than the fluid beneath it. This drives convection, where the downwellings of high salinity pore fluid are co-localized with visible ridges on the surface.

[24], gravel deposits and by encouraging stable salt crust formation [25]. After each inundation-event, the soil is at first saturated with water, which then starts to evaporate on the surface, leaving behind the salt which crystallizes and forms a continuous crust and ridges, once saturation is reached. Crusts both in the managed and unmanaged areas of the lake show well developed polygonal salt ridge patterns.

II. MODEL OF SUBSURFACE CONVECTION

We consider the coupling of surface salt patterns to subsurface flows, as visualised in Fig. 2. Specifically, we treat fluid and salt transport in a saturated porous medium, which is driven by surface evaporation and fed from below by a reservoir of water with some background salinity. The aquifer is assumed to be deep, compared to the ∼1 m diameter of the salt polygons, and any corresponding near-surface dynamics. This system will naturally develop a salinity gradient below the surface, which can become unstable to convective overturning [17–19]. To determine whether field conditions will support such a buoyancy-driven convective instability, we start from mass and momentum balance equations, as are used to describe cases of thermal [17, 26] or solutal [19, 27] convection in porous media. We then use a linear stability analysis of these equations to give the criteria for convective dynamics, and later confirm this instability via direct numerical simulation.

We model the volumetric flux $\boldsymbol{q}$ of a fluid driven by a pressure field p through a porous medium of constant and uniform porosity ϕ and permeability κ. The fluid has a viscosity μ and carries dissolved salt, whose diffusivity D is corrected for the presence of different ions as well as tortuosity (see materials and methods). Using the Boussinesq approximation, buoyancy forces are generated by a variable fluid density $\rho = \rho_b + S\Delta\rho$, where ρ_b is the density of the reservoir fluid, and $\rho_b + \Delta\rho$ is the density at the top boundary; the relative salinity S mediates between the two limits. The model consists of a continuity equation for incompressible fluid flow, Darcy's law and an advection-diffusion equation for salt transport:

$$\boldsymbol{\nabla} \cdot \boldsymbol{q} = 0 \tag{1}$$

$$\boldsymbol{q} = -\frac{\kappa}{\mu}\left[\nabla(p + \rho_b g z) + S\Delta\rho g \hat{\boldsymbol{z}}\right] \tag{2}$$

$$\phi\frac{\partial S}{\partial t} = \phi D \nabla^2 S - \boldsymbol{q} \cdot \nabla S \tag{3}$$

where g is the acceleration due to gravity, and $\hat{\boldsymbol{z}}$ is an upward-pointing unit vector.

Taking the average evaporation rate E as the natural velocity scale for the system, we set the characteristic length and time as $L = D/E$ and $T = D/E^2$, respectively. Non-dimensionalization of Eqs. 1-3 then gives

$$\boldsymbol{\nabla} \cdot \boldsymbol{U} = 0 \tag{4}$$

$$\boldsymbol{U} = -\nabla P - \mathrm{Ra} S \hat{Z} \tag{5}$$

$$\frac{\partial S}{\partial \tau} = \nabla^2 S - \boldsymbol{U} \cdot \nabla S \tag{6}$$

with dimensionless velocity $\boldsymbol{U} = \boldsymbol{q}/\phi E$, time $\tau = tE^2/D$, vertical position $Z = zE/D$ and a modified pressure term, $P = \frac{\kappa}{\phi\mu D}(p + \rho_b g z)$. This system of equations is now scaled only by the Rayleigh number

$$\mathrm{Ra} = \frac{\kappa\Delta\rho g}{\phi\mu E}\ . \tag{7}$$

At the upper surface of the soil, $Z = 0$, we match the vertical flux to the evaporation rate. For salinity, a no-flux boundary condition would correspond to a crust-free scenario, while the presence of a precipitated salt crust sets $S = 1$ there. In this latter case the steady-state solution to Eqs. 4-6, namely $S = \exp(-zE/D)$, represents a salt-rich layer of fluid lying just below the salt crust, and a balance between upwards advection and diffusion back down the salt gradient. This steady state is unstable beyond some critical Rayleigh number, $\mathrm{Ra_c}$, which depends on the upper boundary conditions [17, 18, 28, 29]. For our constant through-flow condition $\mathrm{Ra_c} = 14.35$ for the onset of an instability [18] which leads to down-welling plumes of high salinity. Between $\mathrm{Ra} = 5.66$ and $\mathrm{Ra_c}$ this system of equations may also be unstable to finite amplitude perturbations [18, 19]. The neutral stability curve and most unstable mode of convection relevant to our boundary conditions (see [30] for calculation) are shown in Fig. 3 **A**. At $\mathrm{Ra_c}$ the critical wavenumber $a_c = 0.76$, which corresponds to a wavelength of 1.7 m under typical field conditions.

III. INSTABILITY AND SCALE SELECTION

To determine the Rayleigh numbers relevant to field conditions, and to thus determine if they should lead to a convective instability, we measured the various parameters of Eq. 7 at sites in Owens Lake and Badwater Basin

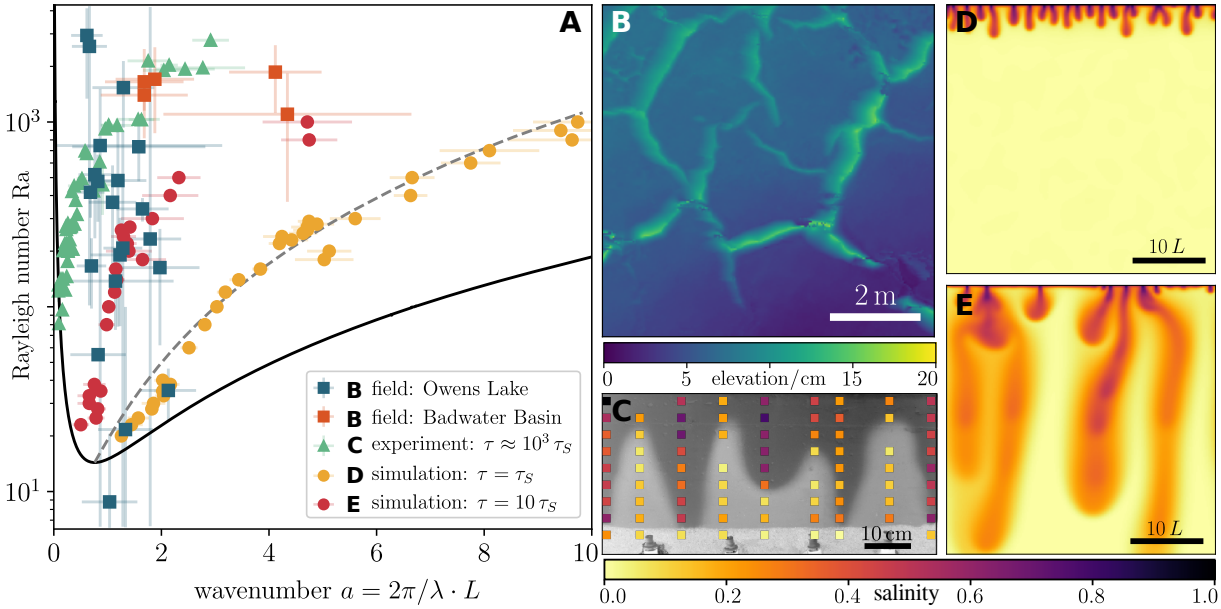

FIG. 3. Characterising the convective instability. **A**: Stability diagram of porous media convection in salt pans. The neutral stability curve (black line) gives the theoretical boundary above which an evaporating stratified pore fluid is unstable to perturbations of wavenumber a. In this region, the most unstable mode (dashed line) gives a prediction of the initial convective wavelength, and its dependence on Ra. Blue and orange squares show values measured in the field at Owens Lake and Badwater Basin respectively via TLS. Yellow and red dots show a measured in simulations at early and late times, respectively, and show coarsening and a reduction of the observed a with time. Green triangles give experimental measurements, and show that coarsening may continue even past this point, over very long timescales. **B** Example TLS surface height profile map at Owens Lake. **C** Convective plumes highlighted by dye in an experimental Hele-Shaw cell are coupled to the salinity, measured at the coloured points by destructive sampling. **D** Example of simulated plumes at early times, $\tau = \tau_S$, are consistent with the most unstable mode, **E** but coarsen by time $\tau = 10\tau_S$.

(see materials and methods for further details). From grain-size distributions measured with a laser particle sizer we calculated d_s, the Sauter diameter [31, 32], of near-surface soil samples; results lay between 4 to 138 μm, representing a fine sand to silt. From this, we estimate porosities ϕ between 0.29 and 0.37, as experimentally reported for similar soils [33]. For relative permeability we use the empirical relationship $\kappa = 0.11\,\phi^{5.6}\,d_s^2$, which is fit to a broad set of experimental and simulated data [34]. Across all sites $\kappa = 6 \cdot 10^{-15}\,\mathrm{m}^2$ to $2 \cdot 10^{-12}\,\mathrm{m}^2$. Next, we measured fluid density differences of $\Delta\rho = 0.21 \pm 0.01\,\mathrm{g/cm}^3$ at Owens Lake, based on differences in the salinity of samples taken from close to the surface and at $\sim 1\,\mathrm{m}$ depth. Evaporation rates of groundwater have been observed to lie in the range of $E = 0.4 \pm 0.1\,\mathrm{mm/day}$ [25, 35] for Owens Lake and $0.3 \pm 0.1\,\mathrm{mm/day}$ [36] for Badwater Basin. Finally, we assume the groundwater's dynamic viscosity to be a constant $\mu = 10^{-3}\,\mathrm{Pa\,s}$.

From these observations we calculated Ra at twenty-one sites around Owens Lake and five in Badwater Basin (all data given in online supplemental material, Table S1). The median values at these two regions were Ra = 237 and 1650 respectively. Values for all 26 sample locations were between Ra = 9 and 2941, and the range of uncertainties for all sites included the case where $\mathrm{Ra} > \mathrm{Ra_c}$. The conditions throughout these patterned salt playa are, therefore, generally suitable to expect a convective overturning of their groundwater, with plumes of high salinity sinking downwards from the surface.

If groundwater convection is linked to salt crust patterning, then their features should express a similar length-scale. Thus, we also measured the surface relief of the salt crust patterns at all sites using a terrestrial laser scanner (TLS, see materials and methods, and Ref. [3]). The crusts show polygonal patterns (e.g. Fig. 3 **B**) with dominant wavelengths ranging from $\lambda = 0.41\,\mathrm{m}$ to $3.02\,\mathrm{m}$. These results are summarised in Fig. 3 **A**, which shows the relationship between Ra and the dimensionless wavenumber $a = 2\pi L/\lambda$ for the field sites (variously coloured squares). The data generally lie above the predicted neutral stability curve of the convection model (black line).However, the pattern wavenumbers measured in the field all lie in a band roughly around the critical wavenumber $a_c = 0.76$, rather than following the Rayleigh number dependency of the most unstable mode predicted for the linear instability that leads to convection (dashed line).

The length-scale, clearly selected by the crust pattern in the field, is instead consistent with a coarsening of the convective plumes after onset of the instability. Coarsening behaviour in related porous media flows is well-

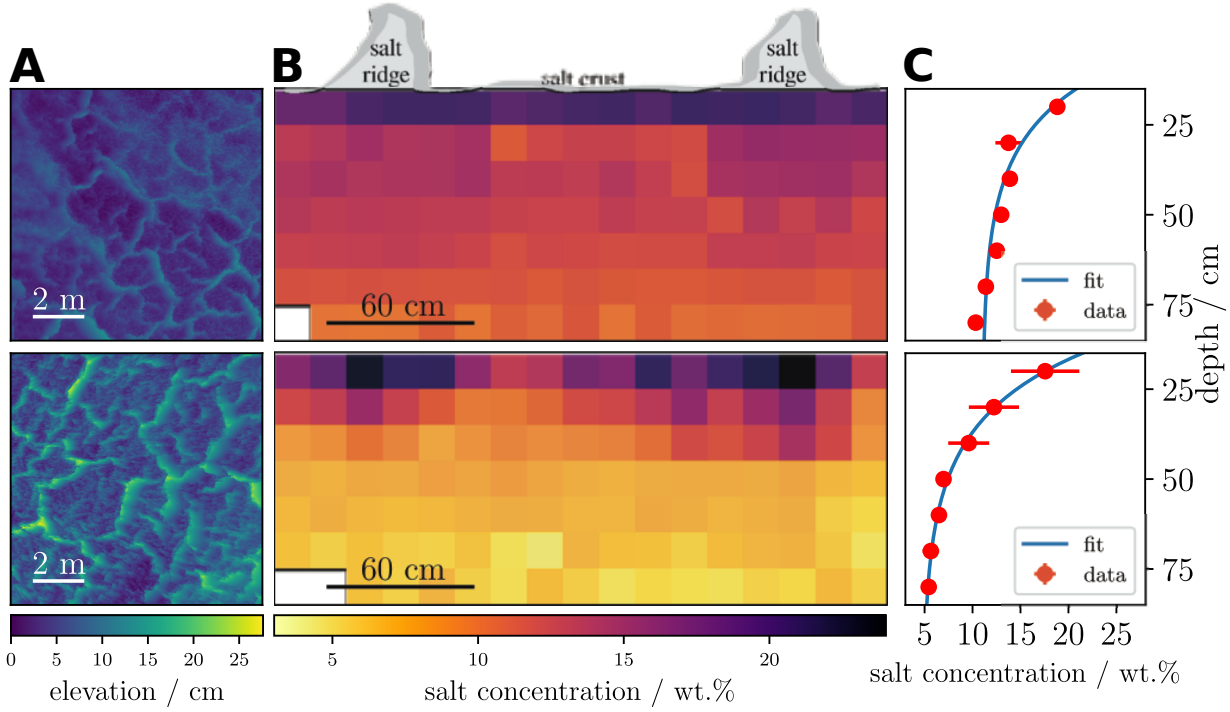

FIG. 4. **A**: TLS scans of the surfaces showing the elevation of ridges above the surface. **B**: Cross-sections of polygons at Owens Lake showing the variation of salt concentration with depth and in-between ridges. Each colored square corresponds to one sample taken at the field site. **C**: Exponential fits to the changing salt concentration with depth.

known [27, 37]. To consider how the convective length-scale evolves with time we simulated Eqs. 4-6 numerically (see Materials and Methods), from Ra = 20 to 1000. The simulations are unstable to convection, which becomes more vigorous with increasing Ra. The initial instability was characterised at a time τ_s, corresponding to when the first salt plume, of salinity $S \geq 0.5$, reached a depth $Z = -1$. The patterns seen at this time (see Fig. 3**C** for a pattern snapshot, and orange dots in Fig. 3**A**) are in good agreement with the most unstable mode predicted by theory. When measured at $10\,\tau_S$, however, many downwelling plumes have merged (see Fig. 3**D**, and red dots in Fig. 3) leading to wavenumbers much closer to the field values, and also clustering around a_c. For our field sites, one year corresponds to $30\,\tau_S$ on average, allowing more than sufficient time for such coarsening to occur during the formation of the salt crust pattern.

Finally, we supplemented our simulations with experiments in a Hele-Shaw cell (similar to e.g. [38, 39]) to explore pattern and wavelength selection in the long-time limit. In the experiment we measured λ and a for systems at times of order $10^3\,\tau_S$. The results are shown in Fig. 3 (green triangles) and suggest that coarsening continues such that values for a outside the initially unstable region are possible. Values measured in the field lie comfortably between the ranges for the timescales explored in the simulations and in the experiments.

IV. DIRECT EVIDENCE FOR CONVECTION

If salt polygon growth is driven by convective dynamics happening beneath the patterns, then horizontal differences in salt concentration should be detectable in the soil, and pore fluid, under typical field and laboratory conditions. To this end, we first dissected an experiment that was undergoing convection, and extracted $\simeq 1$ ml samples from locations along the downwelling and upwelling plumes, from which the salinity was measured. As shown in Fig. 3 **C**, the dynamics of the analogue experiments are clearly driven by, and coupled to, variations in salinity.

From the field, we collected samples of wet soil from two unmanaged sites at Owens Lake (see materials and methods). Surveys of the surface were made, before disturbing each site, by a terrestrial laser scanner, and show the presence of salt polygons of about 2 m in size (Fig. 4 **A**). In each case we sampled along a grid in a cross-section below a polygon. Analysis of the salinity of the samples with respect to pore water content shows very clear evidence for plumes of high salinity sinking down below salt ridges visible at the surface (Fig. 4 **B**). The salinity distribution in an area directly below and up to 30 cm to the left and right of ridges is not correlated with the values measured in the inter-ridge space of the polygon; testing the hypothesis that all values originate in the same distribution we find $p < 0.05$ for for both sites.

The results for the salinity measurements also show an

exponential decay in salinity with depth (Fig. 4, **C**), as is expected for the conditions of buoyancy-driven porous media convection to hold. The natural length scales L recovered from an exponential fit to the salinity gradients, namely $L = 13.5 \pm 5.3\,\mathrm{cm}$ and $L = 17.7 \pm 1.5\,\mathrm{cm}$, match the predicted length scale of $L = D/E \approx 14.3$ cm for Owens Lake.

In summary, not only does analysis of direct field sampling show both horizontal and vertical variations in salt concentration, which support the claim that the system is unstable and convecting, but also that the plumes are also co-localized with the ridges visible on the surface.

V. CONCLUSION

Salt deserts are a common landform important for modeling climate-surface interactions and express a rich repertoire of patterns and dynamics. Here we have shown that, in order to model and understand the surface expression of salt deserts, it is crucial to consider it together with the subsurface dynamics. Specifically, we have explained the emergence of regular salt polygons, which are a common salt crust pattern, as the result of a convection process in the soil underneath. To prove the connection between surface and subsurface, we demonstrated consistent results from theoretical and numerical modeling, analogue experiments and field studies. We are able to explain the onset of pattern formation based on environmental parameters and the length scale expressed by the patterns. As such, we have shown how salt polygons are part of a growing list of geophysical phenomena, such as fairy circles [40, 41], ice wedge polygons [42] and columnar joints [43], which can be successfully explained as the result of the instability of a dynamical process.

ACKNOWLEDGMENTS

The authors thank Grace Holder, of the LADWP, for her generous assistance and support at Owens Lake, and the U.S. National Park Service (Permit DEVA-2016-SCI-0034).

[1] Kennedy K, Bergman R and Johnson R 2017 Star wars: the last jedi Walt Disney Pictures, Lucasfilm
[2] Wadge G, Archer D and Millington A 1994 *Terra Nova* **6** 391–396
[3] Nield J M, King J, Wiggs G F S, Leyland J, Bryant R G, Chiverrell R C, Darby S E, Eckardt F D, Thomas D S G, Vircavs L H and Washington R 2013 *Journal of Geophysical Research: Atmospheres* **118** 12,948–12,961
[4] Nield J M, Bryant R G, Wiggs G F, King J, Thomas D S, Eckardt F D and Washington R 2015 *Geology* **43** 31
[5] Gill T E 1996 *Geomorphology* **17** 207 – 228
[6] Prospero J M 2002 *Reviews of Geophysics* **40**
[7] Fung I Y, Meyn S K, Tegen I, Doney S C, John J G and Bishop J K B 2000 *Global Biogeochemical Cycles* **14** 281–295
[8] Reid J S, Flocchini R G, Cahill T A, Ruth R S and Salgado D P 1994 *Atmospheric Environment* **28** 1699 – 1706
[9] Cahill T A, Gill T E, Reid J S, Gearhart E A and Gillette D A 1996 *Earth Surface Processes and Landforms* **21** 621–639
[10] Ryu J, Gao S, Dahlgren R A and Zierenberg R A 2002 *Geochimica et Cosmochimica Acta* **66** 2981 – 2994
[11] Gill T E, Gillette D A, Niemeyer T and Winn R T 2002 *Nuclear Instruments and Methods in Physics Research Section B: Beam Interactions with Materials and Atoms* **189** 209 – 213
[12] Bryant R and Rainey M 2002 *Remote Sensing of Environment* **82** 360–375
[13] Christiansen F W 1963 *Science* **139** 607–609
[14] Lokier S 2012 *Journal of Arid Environments* **79** 32 – 47
[15] Dellwig L F 1968 *Significant Features of Deposition in the Hutchinson Salt, Kansas, and Their Interpretation* (Geological Society of America)
[16] Tucker R M 1981 *Journal of Sedimentary Research* **51** 779
[17] Wooding R 1960 *Journal of fluid mechanics* **9** 183–192
[18] Homsy G M and Sherwood A E 1976 *AIChE Journal* **22** 168–174
[19] A W R, W T S, Ian W and A A P 1997 *Water Resources Research* **33** 1219–1228
[20] Wooding R A 2007 *Water Resources Research* **43**
[21] Gueler C and Thyne G D 2004 *Journal of Hydrology* **285** 177 – 198
[22] Ryu J, Zierenberg R A, Dahlgren R A and Gao S 2006 *Chemical Geology* **229** 257 – 272
[23] Groeneveld D P and Barz D D 2013 *Open Journal of Modern Hydrology* **03** 241–252
[24] Nicholas L and Andy B 1997 *Earth Surface Processes and Landforms* **23** 69–82
[25] Groeneveld D, Huntington J and Barz D 2010 *Journal of Hydrology* **392** 211 – 218
[26] Wooding R A 1960 *J. Fluid Mech.* **7** 501–515
[27] Slim A C 2014 *Journal of Fluid Mechanics* **741** 461491
[28] Lapwood E R 1948 *Mathematical Proceedings of the Cambridge Philosophical Society* **44** 508521
[29] Horton C W and Rogers F T 1945 *Journal of Applied Physics* **16** 367–370
[30] Ernst M 2017 *Numerical simulation of polygonal patterns in salt playa* Master's thesis University Goettingen URL `http://hdl.handle.net/21.11116/0000-0002-16A7-9`
[31] Sauter J 1928 *VDI-Forschungsheft* **279**
[32] Wang D and Fan L S 2013 2 - particle characterization and behavior relevant to fluidized bed combustion and gasification systems *Fluidized Bed Technologies for Near-Zero Emission Combustion and Gasification* Woodhead Publishing Series in Energy ed Scala F (Woodhead Publishing) pp 42 – 76

[33] DC B and Weyl P 1973 *The American Association of Petroleum Geologists Bulletin* **57**(2) 349–369
[34] Garcia X, Akanji L T, Blunt M J, Matthai S K and Latham J P 2009 *Phys. Rev. E* **80**(2) 021304
[35] Tyler S, Kranz S, Parlange M, Albertson J, Katul G, Cochran G, Lyles B and Holder G 1997 *Journal of Hydrology* **200** 110 – 135
[36] Handford C R 2003 *Water-Resources Investigations Report* **3**
[37] Slim A C, Bandi M M, Miller J C and Mahadevan L 2013 *Physics of Fluids* **25** 024101
[38] Neufeld J A, Hesse M A, Riaz A, Hallworth M A, Tchelepi H A and Huppert H E 2010 *Geophysical Research Letters* **37** L22404
[39] Thomas C, Dehaeck S and Wit A D 2018 *International Journal of Greenhouse Gas Control* **72** 105 – 116
[40] Juergens N 2013 *Science* **339** 1618–1621
[41] Getzin S, Yizhaq H, Bell B, Erickson T E, Postle A C, Katra I, Tzuk O, Zelnik Y R, Wiegand K, Wiegand T and Meron E 2016 *Proceedings of the National Academy of Sciences* **113** 3551–3556
[42] Sletten R S, Hallet B and Fletcher R C 2003 *Journal of Geophysical Resarch* **108** 8044
[43] Goehring L 2013 *Philosophical Transactions of the Royal Society A: Mathematical, Physical and Engineering Sciences* **371** 20120353–20120353
[44] Hollet K J, Danskin W R, McCaffrey W F and Waiti C L 1991 *U.S. Geological Survey*
[45] Annunziata O, Rard J A, Albright J G, Paduano L and Miller D G 2000 *Journal of Chemical & Engineering Data* **45** 936–945
[46] Boudreau B P 2011 *Diagenetic Models and Their Implementation: Modelling Transport and Reactions in Aquatic Sediments* (Springer)
[47] Boudreau B P 1996 *Geochimica et Cosmochimica Acta* **60** 3139–3142
[48] Riaz A and Meiburg E 2003 *J. Fluid Mech.* **494** 95–117
[49] Ruith M and Meiburg E 2000 *J. Fluid Mech.* **420** 225–257
[50] Chen C Y 1998 *Topics in miscible porous media flows* (University of Southern California)

VI. MATERIALS AND METHODS

A. Field

1. *Field site sampling protocol*

Field work was mainly conducted at salt crusts at Owens Lake (CA), in November 2016 and January 2018. See for example [44] for a description of the geology. We collected samples at sites indicated as red dots in Fig. 5 by drawing a core of soil up to a depth of 1 m. The near-surface soil showed normal bedding, indicative of sedimentation following flooding. Soil horizon descriptions are given in the supplement. Samples were collected from each visible layer or with a vertical resolution of at least $\Delta z = 10\,\mathrm{cm}$. Additionally we sampled five sites at Badwater Basin (CA) in November 2016 at a location about 500 m south of the tourist entrance to the area.

At the sites located at 36°47.595′ N 117°91.672′ W and 36°53.864′ N 117°95.277′ W (indicated with orange dots) we additionally dug trenches to take samples along a cross-section below a polygon. Trenches were dug about 200 cm in length, 40 cm in width, down to the water table at $\sim$ 70 cm. Soil samples were taken from a freshly cleaned trench wall in a grid with a spacing of $\Delta x = 15\,\mathrm{cm}$ and $\Delta z = 10\,\mathrm{cm}$. Soil samples had an average volume of approximately 10 cm^3 and were taken using a metal spatula, which was cleaned with distilled water after each use. The samples contained soil with a grain size of medium sand to clay, water and salt, often both dissolved and precipitated. After extraction, samples were immediately stored in water-tight containers, additionally sealed with parafilm.

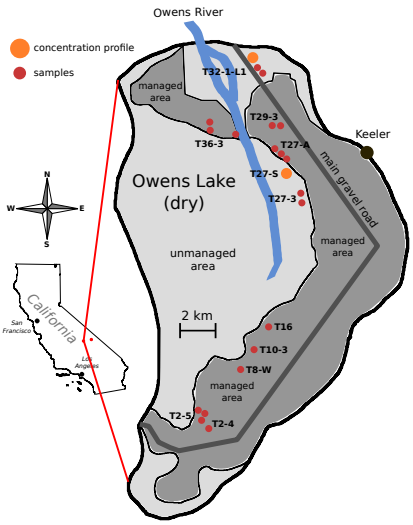

FIG. 5. Schematic map of Owens Lake, CA. Sites at which concentration profiles were created are indicated in orange, other sampling sites in red.

2. *Analysis protocol of field samples*

To determine the salt concentration in each sample collected in the field, the samples were transported from the field to a laboratory equipped with a high precision balance and an oven used to dry the samples. Salt concentration readings used for this publication are based on gravimetric measurements of salt mass compared to pore water mass. Gravimetric analysis of salt concentrations was conducted in the following steps: (1) Extraction of the sample from the containers into a crystallization dish and measurement of the initial weight of the mixture of sand, salt and water. (2) Drying of the sample in an oven at 80°C until all moisture had visibly vanished or for at least 24h followed by weighing to determine the amount of evaporated water. (3) Dilution of the sample with roughly 50 ml of deionized water followed by sedimentation of the solid sample components for approximately

24h and extraction of the liquid part containing the dissolved salt using a syringe. This step was repeated twice. (4) Drying of the solid left behind in the dish and subsequent weighing to determine the amount of salt that was removed from the sample.

3. TLS measurement and analysis protocol

TLS surface scans were obtained using a Leica P20 ScanStation TLS. The TLS was positioned at a height of ~ 2 m, scans of the surface were performed before the surface was disturbed by sampling. Data from the scans was processed following [3]: first data was gridded into a digital elevation map (DEM) with a lateral resolution of $\Delta x = 1\,\mathrm{cm}$ and a vertical resolution of 0.3 mm. Dominant frequencies of surface roughness were then quantified using a two-dimensional Fourier transform of the DEMs. Wavelengths used in this work are the 90th percentile values for ridge wavelengths measured at each field site [4].

4. Measured field parameters

We calculated the Sauter diameter $d_{S,i}$ from the grain size distribution of each sample individually. For the two trench sites we only measured grain sizes for one sample at each depth. Sauter diameter of a field site is then calculated as $d_S = \sum_i d_{S,i}$.
Porosity ϕ was measured by [33] for wet packs of medium, fine and very fine sands similar to our samples. We determined porosity from a linear fit $\phi_i(d_S) = 0.368 - 6\,10^{-4} d_S \frac{1}{\mathrm{m}}$ to the empirical values, where d_S is the Sauter diameter of a sample as described above.
To measure the density difference $\Delta\rho$, we extracted pore water at Owens Lake directly below the surface and at a depth of about 1 m. Density of the pore water was measured using a vibrating-tube densimeter. Since we could not extract water samples from Badwater Basin we use the value of $\Delta\rho$ calculated for Owens Lake as an approximation for the other two locations.
Salt species present in the pore water were determined by quantitative X-ray powder diffraction analysis. Sites at Owens Lake showed a mixture of approximately $53 \pm 7\,\%$ sodium chloride and $30 \pm 5\,\%$ sodium sulfate, as well as traces of other minerals such as natrite, sylvite and burkeite. We base our estimate of D on measurements by [45] for ternary mixtures of the two salts. We calculate D as weighted average of the mole ratios of the two main-term diffusion coefficients of sodium chloride and sodium sulfate $D = (0.83 \cdot 1.5 + 0.17 \cdot 0.74)\,10^{-9}\,\mathrm{m}^2/\mathrm{s} = 1.37\,10^{-9}\,\mathrm{m}^2/\mathrm{s}$ [45].
Since for diffusion processes the tortuosity θ of the porous medium plays a role, we calculate an effective diffusion coefficient $D^* = D/\theta^2 \approx 0.66 \cdot 10^{-9}\,\mathrm{m}^2/\mathrm{s}$ following [46]. The tortuosity is calculated from the porosity as $\theta^2 = 1 - \ln(\phi^2)$ following [47].

5. Estimated field parameters

For the evaporation rate E at both Owens Lake and Badwater Basin we use values found in the literature, which have been measured either by direct measurement or via a temperature based surface energy balance. It has to be noted that the correct determination of E remains a significant source of uncertainty in our modeling which could only be eliminated by accurate measurements of E before and during crust formation.
We estimate viscosity to be $\mu = 10^{-3}\,\mathrm{Pa\ s}$, which is the value for pure water. It has to be noted that viscosity increases by a factor of two between pure water and brine. In parallel, increased salinity also affects the activity of the solution [25] and lowers the evaporation rate. Since the effect of salinity on viscosity and evaporation rate cancel each other in the definition of the Rayleigh number $Ra = \kappa\Delta\rho g/\phi\mu E$, this influence of salinity on viscosity is neglected in our work.

B. Experiments

Experimentally measured wavelengths shown in fig. 3 were obtained from experimental realizations of porous media convection in 2D. Experiments were performed in Hele-Shaw cells of dimensions $40 \times 20 \times 0.8$ cm (width, height, spacing in between plates). The Hele-Shaw cells were filled with artificial sand with a grain diameter of $100 - 200\ \mu$m, a Sauter diameter of $150\,\mu$m and a permeability (measured experimentally) of $\kappa = (1.67 \pm 0.12) \cdot 10^{-11}\ \mathrm{m}^2$. The Hele-Shaw cells were connected to a supply of water mixed with 50 g of sodium chloride per liter, therefore $\Delta\rho = 162\ \mathrm{g/cm}^3$. Evaporation at the top of the cells was controlled by heating and air circulation, evaporation rates were varied in the range of 1 mm/day to 10 cm/day. Porosity $\phi = 0.28 \pm 0.1$ was calculated from a linear fit to values determined by [33] as described above. Kinematic viscosity was again assumed to be constant $\mu = 10^{-3}\,\mathrm{Pa\ s}$, leading to Rayleigh numbers in the range of $\mathrm{Ra} = [80, 2770]$.
Visualization of the convective dynamics in the cells was accomplished by embedding a thin (0.15 cm diameter) perforated metal tube at a depth of approximately 7 cm and injection of dye through the tube. The dye then formed a thin line of color which was advected by the flows inside the cell over time. Dye movement was recorded using time-lapse photography with a standard Nikon SLR camera. Plume spacing was then manually measured in the images using `Fiji`.
An additional experiment was conducted with sand with a grain diameter of $0 - 20\ \mu$m and $d_S = 2\ \mu$m, resulting in $\mathrm{Ra} = (4 \pm 7) \cdot 10^{-3}$ - well below Ra_c. This experiment did not show any convective dynamics.

C. Direct numerical simulation

We numerically solve equations (4) to (6) by employing a stream-function-vorticity approach. We base our methodology on work by [48–50], the detailed implementation is described elsewhere [30]. Specifically we solve the equations by (1) Computing the vorticity from the salinity field using a sixth-order compact finite difference scheme. (2) Solving the Poisson equation for the stream function employing a semi-spectral Fourier-Galerkin method. We accomplish this by transforming the Poisson equation into fourier space and then solving the resulting system of linear differential equations of first order for the stream function. (3) Computing the new velocity field from the stream function by computing the first order spatial derivatives using a sixth-order compact finite difference scheme. (4) Advancing the salinity distribution in time by using an explicit fourth-order Runge-Kutta scheme with adaptive time-stepping.

For the simulations shown in fig. 3 we simulated systems with a uniform evaporation rate and therefore $\frac{\partial \psi(X,Z=0)}{\partial X} = U_Z = 1$, where $\psi(X,Z)$ denotes the stream function. We varied the Rayleigh number between $Ra = 20$ and $Ra = 4000$ and varied the system size (depth $\times$ width in units of natural length L) and resolution from $40L \times 40L$ with $\Delta X = 1.25 \cdot 10^{-1}$ to $10L \times 5L$ with $\Delta X = 1.25 \cdot 10^{-2}$ accordingly.
Measurements shown in fig. (3) are ensemble averages over 6-10 runs. The time τ_S until the salinity at depth $Z = 1$ surpassed 0.5 did not vary significantly between individual runs in one ensemble. Wavenumbers measured at $\tau = 10\,\tau_S$ were recorded at depth $Z = 10$ to capture the coarsened dynamics rather than the small proto-plumes at the surface. We were not able to measure wavelengths at $10\,\tau_S$ in all simulations, especially not for very high Ra. This was due to the high numerical cost as the adaptive timestep had to be very small at high Ra to ensure numerical stability.

View publication stats